Large-scale scours formed by supercritical turbidity currents along the full length of a submarine canyon, northeast South China Sea

Shuang Li [a, b, c], Wei Li [a, b, c*], Tiago M. Alves [d], Jie Sun [a, b, c], Yingci Feng [a, b, c], Jian Li [a, b, c], Shiguo Wu [e]

[a] CAS Key Laboratory of Ocean and Marginal Sea Geology, South China Sea Institute of Oceanology, Chinese Academy of Sciences, Guangzhou 510301, PR China

[b] University of Chinese Academy of Sciences, Beijing 100049, PR China

[c] Innovation Academy of South China Sea Ecology and Environmental Engineering, Chinese Academy of Sciences, Guangzhou 510301, China

[d] 3D Seismic Lab, School of Earth and Ocean Sciences, Cardiff University, Main Building, Park Place, Cardiff, CF10 3AT, United Kingdom

[e] Institute of Deep-sea Science and Engineering, Chinese Academy of Sciences, Sanya 572000, China

Correspondence to Dr. Wei Li (Email: wli@scsio.ac.cn)

Abstract

High-resolution multi-beam bathymetric and seismic data enables a detailed morphological investigation of a submarine canyon (West Penghu Canyon) on the northeastern South China Sea margin, where twenty-three (23) scours are observed along the canyon thalweg. These scours form narrow topographic depressions in plan view and show asymmetrical morphologies in cross-section. The identified scours can be further divided into two groups (Type A and B scours) based on their sizes and relative locations. They are separated by a slope break at a water depth of ~2850 m. Type A scours (S1-S18) occur upslope from the slope break, whereas Type B scours (S19-S23) lie downslope from this same break. The scours are interpreted as net-erosional cyclic steps associated with turbidity currents flowing through the West Penghu Canyon; the currents that form Type A scours reveal higher

V, Q, and Δ_{el} compared to Type B scours. A change in slope gradient and loss of lateral confinement are proposed to control the change from Type A to Type B scours. Furthermore, Coriolis force influences the flow direction of turbidity currents, leading to the preferential development and larger incisional depths of scours towards the southwestern flank of the West Penghu Canyon. Our results contribute to a better understanding on the origin of scours in submarine canyons across the world.

Keywords: South China Sea; Scours; Cyclic steps; Submarine canyon; Geomorphology; Coriolis force.

1 Introduction

Deep-water sedimentary processes, including gravity-driven downslope and along-slope processes, play a vital role in the shaping of continental margins (Rebesco et al., 2014; Mosher et al., 2017). Gravity-driven downslope sedimentary processes include a range of physical processes ranging from slides, slumps, and cohesive debris flows, which are able to form turbidity currents (Talling et al., 2012). Turbidity currents are themselves one of the most important processes transporting large volume (hundreds of km^3) of sediment downslope from the continental slope into deep-marine environments (Paull et al., 2002; Talling et al., 2007). The morphology of continental margins can be modified by turbidity currents, leading to the generation of submarine canyons, channels, sediment waves and scours (Cartigny et al., 2014; Covault et al., 2014). Turbidity currents and related seafloor morphological features have been proposed to be fundamentally significant to channel initiation (Mchargue et al., 1991; Covault et al., 2014; Covault et al., 2017).

Cyclic steps are long-wave, upstream-migrating, upper-flow-regime bedforms bounded by

internal hydraulic jumps in turbidity currents (Covault et al., 2017). They are generally divided into two categories: net-depositional and net-erosional cyclic steps (Fildani et al., 2006; Lamb et al., 2008; Kostic, 2011; Covault et al., 2014; Postma and Cartigny, 2014; Zhong et al., 2015; Li and Gong, 2018). Net-depositional cyclic steps take the form of upstream-migrating sediment waves relative to submarine channels (Fildani et al., 2006; Kostic et al., 2010; Cartigny et al., 2011; Kostic, 2011), while net-erosional cyclic steps are developed as trains of upstream-migrating scours (Kostic, 2011; Maier et al., 2011; Symons et al., 2016). Net-erosional cyclic steps (scours) are crescent-shaped to enclosed depressions that cut into the sea floor and have been identified in many a submarine canyon and channel, e.g. the Setúbal Canyon in West Iberia (Wynn et al., 2002), the Monterey East System in California (Fildani et al., 2006) and the Lucia Chica channel off central California (Maier et al., 2013). Net-erosional cyclic steps (scours) show closed topographic depressions, disrupted and discontinuous internal architecture, and less asymmetrical cross-sectional morphologies, stronger up-current migration than net-depositional cyclic steps (sediment waves).

The flow properties of turbidity currents generating the scours have been investigated by numerical stimulations (e.g. Fildani et al., 2006; Spinewine et al., 2009; Kostic, 2011) and physical experiments (e.g. Cartigny et al., 2014; Vellinga et al., 2017). Moreover, Li and Gong (2018) have quantitatively analyzed the difference between net-erosional cyclic steps (scours) and net-depositional cyclic steps (sediment waves). Turbidity currents flowing through net-erosional cyclic steps (scours) exhibit relatively higher flow velocity, bankfull discharge, and energy loss of hydraulic jump than net-depostional cyclic steps (sediment waves).

In contrast to the previous literature, this work focus on net-erosional cyclic steps developed along the full length of a submarine canyon, the West Penghu Canyon of the South China Sea (Figs.1

and 2). Here, a submarine canyon system, including nine N-S oriented submarine canyons, have been previously documented within the Taixinan Basin (Yin et al., 2015) (Fig. 2). High-frequency occurrences of turbidity currents have been reported in this region and related to high sediment supply (Murray et al., 2004; Ding et al., 2013), frequent earthquakes (Liu et al., 1999; Hsu et al., 2008; Gavey et al., 2016) and seasonal typhoons (Zhang et al., 2018). The study area is located in the northeastern part of the Taixinan Basin (Fig. 1), where the water depth ranges from 200 to 3400 m (Fig. 2). Zhong et al. (2015) have reported and investigated similar scours along the Taiwan Canyon and the West Penghu Canyon, and these scours were interpreted as cyclic steps. In this study, we find that the scours are distributed along the full length of the West Penghu Canyon, and its upper and middle reaches show much smaller scours than the lower reach. Scours on the lower reach also developed more closely to the southwest flank of the canyon (Figs. 3 to 6). As the flow properties of turbidity currents generating the scours in the West Penghu Canyon are still poorly understood, we undertook a quantitative analysis of these features using high-resolution multibeam bathymetric and multichannel seismic data, so that:

(a) The morphology and geometrical parameters of seafloor scours along a large submarine canyon could be investigated;

(b) The flow properties of turbidity currents crossing the scours could be determined;

(c) The factors controlling morphology changes of different types of scours were confirmed;

(d) The ways the Coriolis force affects the scours' distribution and development could be discussed in this work.

2 Geological setting

The South China Sea (SCS) is one of the largest marginal seas in the Pacific Ocean. It was first generated from Eocene to Middle Miocene (33-15.5 Ma) due to continental rifting from and subsequent seafloor spreading (Wang and Li, 2009; Li et al., 2014). Arc-continent collision between the Luzon Arc and the northern South China Sea margin around Taiwan, between the latest late Miocene and the early Pliocene, relates to an important regional tectonic event (Bowin et al., 1978; Suppe, 1981; Sibuet and Hsu, 1997). At the time, the eastern part of SCS was subducted under the Luzon Arc, generating the N-S oriented Manila Trench (Taylor and Hayes, 1983; Pautot et al., 1986). To the west, the SCS became bounded by a strike-slip fault zone offshore Vietnam (Taylor and Hayes, 1983). As a result of this tectonic evolution, several sedimentary basins occur at present in the northern continental margin of South China Sea. From east to west, they are the Taixinan, Pearl River Mouth, Qiongdongnan and Yinggehai Basins (Xie et al., 2006).

The Taixinan Basin is bounded by the Dongsha Islands to the west and the Taiwan Island to the east (Fig. 1). It extends across the northern South China Sea and the south-western Taiwan continental slope (Fig. 1). Four major structural features, including the Northern Depression, the Central High, the Southern Depression, and the Southern High, are identified within the basin (Du, 1994; Lin et al., 2008). The basement of the basin is composed of Cretaceous sandstones, siltstones and shales deposited prior to the Cenozoic. In the Cenozoic, the basin was filled with Oligocene–Miocene shelf sandstones and mudstones, Pliocene shelf to deep-sea sandstones and mudstones, and Pleistocene deep-sea muds intercalated with sands and silts (Lee et al., 1993; Yu and Chen et al., 1994).

In the study area, a submarine canyon system consisting of nine (9) parallel submarine canyons comprise the most obvious bathymetric features on the northeast South China Sea (Zhong et al., 2015).

The West Penghu Canyon is located in the northwestern part of the Taixinan Basin (Fig. 2), with the Penghu High to the north and the Manila Trench to the south.

3 Data and methods

High-quality multibeam bathymetric and multichannel seismic data imaging the West Penghu Canyon in its whole length are used as the primary dataset in this work. The multibeam bathymetric data was imported and analyzed in the Global Mapper® software. A two-dimensional (2D) multichannel seismic profile was recently acquired by the South China Sea Institute of Oceanology, Chinese Academy of Sciences on May, 2019 using an 1800 m-long streamer with 144 channels. This acquisition geometry produced seismic traces with a spacing of 12.5 m. The frequency bandwidth of the seismic data is 30–45 Hz, providing an average vertical resolution of 11-17 m for the shallow strata. The data were processed using RadExpro® and interpreted using Geoframe®.

In this study, the bankfull flow properties of turbidity currents flowing along the West Penghu Canyon were calculated based on the morphological parameters of the interpreted canyon and associated scours. These morphological parameters include the wavelength, wave height, length and slope gradient of lee/stoss side of scours, and the bankfull depth and width of the West Penghu Canyon (Fig. 7b). These morphological parameters were used in several equations to calculate the flow properties of turbidity currents flowing through each scour, including the velocity (V), discharge (Q), Froude number (F_r) and loss energy in the hydraulic jumps (Δ_{el}). Three parts are considered when the turbidity currents flow through a single scour: (1) at the base of the lee side just before the hydraulic jump, (2) at the crest of the scour, and (3) at the base of the stoss side just after the hydraulic jump (Fig. 7b). Parts (1) and (3) can be computed by Equations (1) to (7) derived from Konsoer (2013),

while part (2) of our computation derives from Equations (8) to (10) from Chanson et al (2004) (See supplementary material). The volume sediment concentration (C) ranges from 0.2% to 0.6%, and the coefficient of friction at the bedforms (f) is between 0.002 and 0.005 (Konsoer et al., 2013). We use a volume sediment concentration of 0.2%, and a friction coefficient of 0.005, as the best fits for both river and submarine environments (Konsoer et al., 2013). Other important parameters were gathered from Konsoer et al (2013) such as the gravitational acceleration (g=9.81 m^2/s), the Richardson number (R=1.65), and the slope of the canyon (S=0.017).

4. Results

4.1 Scours along the West Penghu Canyon

The West Penghu Canyon is located in the northeastern part of the interpreted bathymetric map and has a NW-SE orientation. It is 90-km long and occurs at a depth between 400 m to 2950 m in depth (Fig. 2). The width of the West Penghu Canyon varies from 5 to 10 km. A total of 23 scours have been identified along the West Penghu Canyon, comprising fully enclosed depressions with crescent-shaped crests at a water depth ranging from 2145 m to 2950 m (Figs. 5b and 6b). Most of the scours develop close to the southwestern flank of the West Penghu Canyon (Fig. 3a). A slope break can be distinguished at a water depth from 2845 m to 2865 m, showing an average slope gradient of 0.02°(Figs. 3a, b and c). Based on their location and sizes, the scours along the West Penghu Canyon can be classified in two types: a) scours developed in the upper reach of the slope break (Type A), and b) those located in the lower reach of the slope break, herein named Type B scours (Figs. 3a and b). The slope gradients of the stoss sides of the scours (α) range from 1.11° to 6.41°, with a mean value of 2.69°, while the slope gradient of their lee sides (β) range from 0.42° to

2.64°, or 1.23° on average (Fig. 8c). Scour asymmetry (A_y) returns values of 0.18 to 2.02, with a mean value of 0.78 (Fig. 8b). W/H (wave length/ wave height) ratios increase when changing from Type A to Type B scours (Table 1; Fig. 8a).

4.1.1 Type A scours

Type A scours occur in the upper and middle reaches of the West Penghu Canyon, at water depths from 2145 m to 2845 m, with an average slope gradient of 1.25°. Type A scours show a wavelength of 1.3-3.3 km and are 17-146 m high (Table 1). The length of the stoss side of Type A scours (L_{stoss}) ranges from 370 m to 1172 m, with a mean value of 771 m. The length of the lee side of Type A scours (L_{lee}) ranges from 459 m to 2306 m, for an average of 1409 m (Table 1). The slope gradient of the stoss side of Type A scours (α) ranges from of 1.11° to 6.41° for a mean value of 2.69°, while the slope gradient of their lee side (β) ranges from of 0.42° to 2.64°, with a mean value of 1.23° (Fig. 8c). The values of asymmetry (A_y) of Type A scours range from 0.18 to 1.29, with 0.74 on average (Table 1; Fig. 8b). Seismic profiles show that Type A scours S5 to S9 have obvious truncations reflections in both their stoss and lee sides (Figs. 4a and b).

Two trains of scours (S4-S14) can be distinguished in the upper reach of the West Penghu Canyon (Fig. 5). They are separated by a positive bathymetric feature (an intra-canyon high) at water depths between 2272 m and 2612 m (Fig. 5a). On the bathymetric profiles, the scours to the southwest have larger incision depths than their counterparts to the northeast. The differences in depth between parts of these scours are 25 m, 30 m and 16 m, respectively (Table 3).

4.1.2 Type B scours

Type B scours are located in the lower reach of the West Penghu Canyon at a water depth from

2865 m to 2950 m, in a region with an average slope gradient of 0.38°. Type B scours have wavelengths of 1.5-4.7 km and are 30-93 m high (Table 1). The length of the stoss side of Type B scours (L_{stoss}) ranges from 876 m to 2381 m, with a mean value of 1718 m. The length of the lee side of Type B scours (L_{lee}) is 603 m to 2349 m, for an average of 1374 m (Table 1). The slope gradient of the stoss side of Type B scours (α) ranges from 1.02° to 3.16°, with a mean value of 2.09°, while the slope gradient of the lee side (β) ranges from 0.9° to 1.53°, with a mean value of 1.22° (Fig. 8c). The values of asymmetry (A_y) of Type B scours range from 0.78 to 2.03, with an average of 1.41 (Table 1; Fig. 8b). On seismic profiles, Type B scours S19 to S23 show trains of upstream-migrating scours (Fig. 4a). Cross-section profiles show sub-parallel or parallel reflections draping each of the five scours (Figs. 4a and c). Truncated reflections can be observed in their lee sides and minor upstream accretion occurs in their stoss sides (Figs. 4a and c).

4.2 Flow properties of turbidity currents generating the scours

Flow properties of turbidity currents along the West Penghu Canyon are calculated using Equations (1) to (7) based on the scours' morphological characters. The flow velocity of turbidity currents before hydraulic jumps occur (V_1) ranges from 5.4 m/s to 11.8 m/s (8.8 m/s on average) (Table 2; Fig. 9a). The flow discharge of turbidity currents before the hydraulic jumps (Q_1) ranges from 7.2×10^5 m^3/s to 3.8×10^7 m^3/s (Table 2; Fig. 9b), and Fr_1 is a stable value (2.13) with a small change (Table 2; Fig. 9c).

The V_1 and H_1 of turbidity currents were used in Equations (8) to (10) to compute V_2 (flow velocity after hydraulic jumps), H_2 (flow depth post hydraulic jumps) and Fr_2 (Froude number of turbidity currents during hydraulic jumps). The velocity of the turbidity currents after the hydraulic

194 jumps (V_2) ranges from 2.8 m/s to 8.8 m/s, with a mean value of 6.6 m/s, and Fr_2 is a stable value
195 ranging between 0.5 and 0.6 (Table 2; Figs. 9a, b and c). The loss of energy recorded by the turbidity
196 currents during the hydraulic jumps (Δ_{el}) can be calculated by equation 11. It ranges from 0.6 m and
197 6.2 m with a mean value of 3.6 m (Table 2; Fig. 9d). The flow properties of turbidity currents on the
198 crest of these scours (V_3, Q_3, Fr_3) can also be calculated by Equations (1) to (7). Here, V_3 ranges from
199 2.4 m/s and 11.6 m/s (averaging 7.9 m/s), Q_3 ranges from 5.1×10^5 m^3/s and 3.5×10^7 m^3/s (averaging
200 1.7×10^7 m^3/s) and Fr_3 is 2.13 (Table 2; Figs. 9a, b and c).

201 Before the hydraulic jumps, the velocity of turbidity currents flowing through Type A scours (V_1)
202 ranges from 7.8 m/s to 11.8 m/s (averaging 9.8 m/s) (Table 2; Fig. 9a). The flow discharge of turbidity
203 currents flowing through Type A scours (Q_1) ranges from 1.1×10^7 m^3/s to 3.8×10^7 m^3/s (Table 2; Fig.
204 9b). Importantly, there is a significant decrease in the velocity (V) and discharge (Q) of turbidity
205 currents when comparing Type A with Type B scours. The velocity of turbidity currents flowing
206 through Type B scours (V_1) ranges from 3.8 m/s to 5.8 m/s (4.8 m/s on average) (Table 2; Fig. 9a).
207 The flow discharge of turbidity currents flowing through Type B scours (Q_1) ranges from 7.3×10^5
208 m^3/s to 3.9×10^6 m^3/s (Table 2; Fig. 9b). Immediately after the hydraulic jumps, the velocity of turbidity
209 currents flowing through Type B scours (V_2) ranges from 5.8 m/s to 8.8 m/s (averaging 7.3 m/s)
210 (Table 2; Fig. 9a).

211 The loss of energy in turbidity currents during hydraulic jumps (Δ_{el}) can be calculated by
212 Equation 11, and range from 2.7 m and 6.2 m with a mean value of 4.5 m (Table 2; Fig. 9d). An
213 obvious decrease in the velocity of turbidity currents after the hydraulic jumps, and a loss energy of
214 turbidity currents during these same jumps, can be observed at the limit between Type A and Type B
215 scours. Here, the velocity of turbidity currents flowing through Type B scours (V_2) ranges from 2.8

m/s to 4.3 m/s (3.6 m/s in average) (Table 2; Fig. 9a). The loss of energy in turbidity currents during hydraulic jumps (Δ_{el}) of Type B scours ranges from 0.6 m and 1.5 m with a mean value of 1.1 m (Table 2; Fig. 9d). In the third stage, the values of flow properties of turbidity currents on the crests of Type A scours (V_3, Q_3) range from 7.4 m/s to 11.6 m/s (9.5 m/s in average) and from 1×10^7 m^3/s to 3.5×10^7 m^3/s (2.8×10^7 m^3/s in average), respectively.

In the transition from Type A to B scours, the flow conditions of turbidity currents also show an obvious decrease. The velocity of turbidity currents on the crests of Type B scours (V_3) ranges from 2.4 m/s to 3.4 m/s (2.9 m/s in average). The flow discharge of turbidity currents on the crests of Type B scours (Q_3) ranges from $5.1\times10^5 m^3/s$ to 8.2×10^6 m^3/s, averaging 4.4×10^6 m^3/s (Table 2; Figs. 9a, b and c).

4.3 Differences in morphological and hydraulic properties between Type A and B scours

The wavelengths of Type A scours are 1-1.5 times larger than Type B scours, while the waveheights of the Type A scours are 0.2-0.6 times smaller than Type B scours (Table 1). The length of the stoss side of Type B scours (L_{stoss}) is 2.3-6.4 times longer than Type A scours, while the length of the lee side (L_{lee}) and the full length of Type B scours are 1-5.4 times and 1.4-3.5 times, respectively (Table 1). The slope gradient of the stoss side of Type A scours (α) is 1-2 times larger than Type B scours, while the slope gradient of the lee side (β) of Type A scours is 1.7-2.9 times larger than Type B scours. The values of asymmetry (A_y) of Type B scours are 1.6-4.3 times larger than Type A scours (Table 1). In terms of their hydraulic characteristics, values of V1, Q1, and Δel for turbidity currents forming Type A scours (S1 to S18) are 1-3 times, 13-50 times, and 4-6 times larger than those forming Type B scours (S19 to S23), respectively.

5. Discussion

5.1 Origin of the scours along the West Penghu Canyon

In this study, 23 scours have been identified along the West Penghu Canyon; they all form fully enclosed depressions with crescent-shaped crests (Figs. 3a, b and c). Symons et al. (2016) have conducted a statistical analysis on a number of scours spanning a broad range of water depths and environments. In the study area, the wavelengths and wave heights of the scours are comparable to the large-scale scours documented in Symons et al. (2016) (see Fig. 10). We find that these scours comprise large-scale erosional bedforms, but their origin is still not clear.

Scours within submarine canyons have been related to supercritical turbidity currents and associated hydraulic jumps (Fidani et al., 2006; Symons et al., 2016; Hage et al., 2018). Numerical and physical modelling has confirmed that hydraulic jumps occur along the flow paths of turbidity currents captured by submarine canyons (Fildani et al., 2006; Kostic and Parker, 2006; Postma et al., 2009; Kostic, 2011; Cartigny et al., 2011;). The formation of scours is determined by the occurrence of hydraulic jumps, where a flow makes a rapid transition from a thin, rapid supercritical flow (Froude number > 1) to a thick, slow subcritical flow (Froude number < 1) (Fildani et al., 2006; Normark et al., 2009). In this study, 23 scours along the West Penghu Canyon show continuous changes in Froude number (Fig. 9), indicating that the scours are linked to the formation of hydraulic jumps. Therefore, the formation of the large-scale scours along the West Penghu Canyon can be attributed to the transition from supercritical to subcritical turbidity currents.

After the concept of supercritical and subcritical flows was introduced (Kostic and Parker et al., 2006; Fildani et al., 2006; Lamb et al., 2008), most scours in submarine canyons and channels were

identified as net-erosional cyclic steps (e.g., Kostic, 2011). For instance, Zhong et al. (2015) grouped the scours along the West Penghu Canyon into two main categories. They considered our Type A scours (S1 to S18) as net-erosional cyclic steps, while Type B scours (S19-S23), identified downslope from the slope break, were net-depositional cyclic steps according to Zhong et al. (2015). This work shows these scours to be enclosed depressions on the contour maps (Figs. 5c and 6c), forming trains of asymmetrical waveforms in a characteristic upslope migration in cross-section (Figs. 3c and 4c). The multichannel seismic profiles in this work also show truncations in some scours (S5-S7; S19-S23), suggesting erosion of seafloor sediment (Figs. 4a, b and c). This latter character indicates that scours are all bounded by hydraulic jumps of overriding, alternating Froude-supercritical to subcritical turbidity currents; loss of strata is attributed to erosion by turbidity currents (Covault et al., 2014). The scours identified in this study are similar to those documented along the Monterey East Channel, which are interpreted as net-erosional cyclic steps (Fildani et al., 2006; Symons et al., 2016). Thus, we think Type A and B scours should be interpreted as net-erosional cyclic steps.

5.2 Factors controlling the shift from Type A to Type B scours

The large-scale scours in the study area could be divided into two main types (Type A and B) based on their locations and sizes (Figs. 3a and b). Type A scours are observed in the upper reach of the West Penghu Canyon (Fig. 5), while Type B scours develop in the lower reach (Fig. 5). In plan view, Type A scours are much smaller compared to Type B scours (Figs. 3a, 3b and 4a). On the cross-section profile, Type A scours have an average slope gradient of 1.25°, while Type B scours have a slope gradient of only 0.38° on average (Fig. 3c). In detail, the flow properties of turbidity currents crossing Type A and B scours show a pronounced decrease in the flow velocity (11.8 m/s to 3.1m/s),

279 flow discharge (from 3.8×10^7 m^3/s to $5.1\times10^5 m^3/s$) and loss of energy (from 6.17 to 0.63) (Fig. 9;
280 Table 2). Such a dramatic change in the properties of turbidity currents has seldom been documented
281 in submarine canyons and channels, and raises questions about the true physical factors controlling
282 the transition from Type A to Type B scours.

283 Factors such as slope gradient, sediment concentration, bed roughness and entrainment
284 coefficient, have been considered to play a vital role in changing the flow regimes of turbidity currents
285 in submarine canyons (Kostic and Parker 2006; Kostic 2011). Variations of slope steepness can result
286 in the changes in both the dominant erosion process and the controlling sediment regime along
287 submarine canyons (Huang and Laflen, 1996; Gabbard et al., 1998; Huang, 1998). The presence of a
288 slope break in the West Penghu Canyon may also lead to the decrease of flow velocity, discharge and
289 energy loss of turbidity currents (Figs. 9a, c and d). As a consequence of such a slope break, the
290 erosional capacity of turbidity currents may be reduced, explaining why Type A scours have smaller
291 wavelengths and larger wave heights than Type B scours (Fig. 8). Therefore, we propose that the
292 change of slope gradient (due to the presence of the slope break) has a marked effect on the change
293 from Type A to Type B scours along the West Penghu Canyon.

294 The relationship between morphologies of scours (L_{stoss} and A_y) and properties of turbidity
295 currents (V_1, Q_1 and Δ_{el}) are shown in Figure 11. The power law relationships amongst L_{stoss} and V_1,
296 Q_1, and Δ_{el} show average correlation coefficient (R^2) values of 0.356to 0.401 (Figs. 11a,11d and 11g).
297 The relationship amongst A_y and V_1, Q_1 and Δ_{el} also reveals an average correlation coefficient, with
298 Type A scours showing less asymmetry than Type B scours (Figs. 11b, 11d and 11h). Plots of W_1/H_1
299 against V_1, Q_1 and Δ_{el} show clear power law relationships with R2 values close of above 0.9 (Figs.
300 11c, 11f and 11i). The dramatic change in V_1, Q_1 and Δ_{el} of turbidity currents downstream suggests a

decrease in the sediment-transport capacity of turbidity currents, a change associated in this work to the presence of the slope break previously mentioned. This downstream decrease in V_1, Q_1 and Δ_{el} probably drives the progressive change in morphological characteristics of scours, including the observed increase in L_{stoss}, A_y and W_1/H_1 downstream (Li and Gong et al., 2018).

Recent physical experiments have shown that abrupt loses in the lateral confinement of canyons can lead to flow relaxation and a decrease in flow velocity (de Leeuw et al., 2016; Pohl et al., 2019). Moreover, spatial and temporal variations in flow velocity affect the ability of turbidity flows to transport sediment (de Leeuw et al., 2016). In our case, Type A scours (S1-S18) develop within a narrow area (~3.6 km in width) in the West Penghu Canyon, and Type B scours (S19-S23) are distributed in a wider area (~5.5 km in width) (Figs. 3, 5, 6). The levee height of the canyon flanks ranges from 182 m to 463 m in the upper canyon reach where the Type A scours occur. Conversely, it ranges from 19 m to 110 m in the lower canyon reach where the Type B scours are observed (Table 1). We postulate that the increase in canyon width and the decrease in the height of canyon flanks led to the loss of lateral support for turbidity currents. Lateral spreading and thinning thus occur in the lower reach of the West Penghu Canyon, correlating with a dramatic change in the flow regime of turbidity currents crossing from Type A to Type B scours (Figs. 9a, c and d). The erosional depths of Type B scours are smaller compared to Type A, a character that can be correlated with a decrease in the velocity of turbidity currents.

In summary, we propose that both the change of slope gradient and the loss of lateral confinement are main controls on the flow properties of turbidity currents, and have led to the change from Type A to Type B scours in the West Penghu Canyon.

5.3 The role of Coriolis force on the distribution and development of scours

The Coriolis force acts as a complementary centrifugal force in the world's oceans and seas, changing the direction of a moving body to the right in the Northern Hemisphere and to the left in the Southern Hemisphere (Persson et al., 1998; Persson et al., 2000). The effect of the Coriolis force upon turbidity currents has been identified in previous numerical simulations and physical experiments (e.g. Jones et al. 2006; Wells, 2009; Cossu et al., 2010). Wells (2009) proposed that if turbidity currents traverse a large distance in a time-scale comparable to one day, then the Coriolis force will result in a significant deflection of the turbidity currents to the right in the Northern hemisphere. If the turbidity currents flow towards the south, it would result in more erosion on the western margin of the canyons, and more deposition on the eastern counterpart (Cossu and wells, 2013). The importance of Coriolis forces affecting turbidity currents can be expressed with the Rossby number (Cossu and Well et al., 2013). Coriolis forces can play a key role in controlling the morphology of submarine canyons when Rossby numbers are small ($R_0 < 10$) (Cossu et al., 2010).

The calculated Rossby numbers for the West Penghu Canyon range from 10 to 21.6, suggesting that the Coriolis force does not play a significant role on the flow direction of turbidity currents. However, two trains of scours (S4-S14) can be distinguished in the upper reach of the West Penghu Canyon (Figs. 5a, b and c). They are separated by a positive bathymetric feature (an intra-canyon high), which is located at a water depth of 2272 m to 2612 m (Figs. 5a and 13a). This intra-canyon high is ~10 km in length, 2 km in width and 30–120 m in height (Zhong et al., 2015; Figs. 12a, b and c). According to our interpretation, turbidity currents can be split into two branches when meeting the intra-canyon high, leading to the formation of two trains of scours in the upper reach of the West Penghu Canyon. Based on the bathymetric profiles in this work, the southwest train of scours has a

larger incised depth to the one to the northeast (Figs. 13a, b and c). In order to explain this phenomenon, one needs to consider that turbidity currents flowing through the West Penghu Canyon are deviated to the southwest due to the Coriolis force. This leads to more erosion and larger incised depths in the southwest side of the intra-canyon high.

The scours in the middle and lower reaches of the West Penghu Canyon are distributed close to the southwest canyon flank (Figs. 6a, b and c). Bathymetric isobaths adjacent to this flank are closer together than those on the northeast flank (Fig. 6c). This indicates that the southwest canyon flank is relatively (and frequently) more eroded by turbidity currents. When flowing through the middle and lower reaches of the canyon, turbidity currents are forced to the southwest and erode the southwest flank of the canyon. This explains why this latter flank is much steeper and more scours develop on it (Fig. 14).

6 Conclusions

High-resolution bathymetric and seismic data allow us to investigate the origin, transition and development of scours along the full length of the West Penghu Canyon, northeastern South China Sea. The main conclusions of this work are as follows:

(1) Twenty-three (23) scours have been identified along the thalweg of West Penghu canyon, northeast continental slope of South China Sea. These scours can be sub-divided into two types, Type A and Type B, based on their locations and sizes.

(2) These scours are revealed as closed topographic depressions in plan view and show asymmetrical morphologies in cross-section. The origin of these scours is related to the strength of turbidity currents flowing through the West Penghu Canyon. They are all interpreted as net-erosional

cyclic steps.

(3) Type A scours are more symmetric, show a wider range in slope angle (α, β, θ), larger wave heights and smaller wavelengths, when compared to Type B scours. Turbidity currents flowing through Type A scours reflect higher V (flow velocity), Q (flow discharge), and Δ_{el} (energy loss of hydraulic jump) than those crossing Type B scours.

(4) The main factors controlling the observed shift from Type A to B scours are the presence of slope break in the middle of the canyon (2845 m-2865 m) and the loss of lateral confinement of the canyon.

(5) The Coriolis force is revealed as a prominent influence on the deflection of turbidity currents to the southwest. Therefore, several Type A scours located in the west of the intra-canyon high show larger incision depths than those in the east. Moreover, more scours occur close to the southwest flank of the West Penghu canyon.

Acknowledgements

This work was financially supported by the National Scientific Foundation of China (Grant No. 41876054). Dr. Wei Li is funded by the CAS Pioneer Hundred Talents Program. Dr. Matthieu Cartigny and Dr. Jacob Covault are thanked for their suggestions on an earlier version of this manuscript. This paper benefited from constructive comments by the Editor and reviewers.

References

Arzola, R.G., Wynn, R.B., Lastras, G., Masson, D.G., Weaver, P. P. E., 2008. Sedimentary features and processes in the Nazaré and Setúbal submarine canyons, west Iberian margin. Marine Geology. 250, 64-88.

385 Bowin, C., Lu, S.R., Lee, C.S., Schouten, H., 1978. Plate Convergence and Accretion in Taiwan-Luzon Region. AAPG
386 Bulletin (American Association of Petroleum Geologists). 62, 1645-1672.
387 Cartigny, M.J.B., Ventra, D., Postma, G., van Den Berg, J.H., Venditti, J., 2014. Morphodynamics and sedimentary
388 structures of bedforms under supercritical-flow conditions: New insights from flume experiments. Sedimentology.
389 61, 712-748.
390 Cartigny, M.J.B., Postma, G., van den Berg, J.H., Mastbergen, D.R., 2011. A comparative study of sediment waves
391 and cyclic steps based on geometries, internal structures and numerical modeling. Marine Geology. 280, 40-56.
392 Chanson, H., 2004. Hydraulics of Open Channel Flow, An Introduction Basic Principles, Sediment Motion, Hydraulic
393 Modelling. Design of Hydraulic Structure, Butterworth-Heinemann, Oxford, UK. p. 53–63.
394 Cossu, R., Wells, M., Wahlin, A., 2010. Influence of the Coriolis force on the velocity structure of gravity currents in
395 straight submarine channel systems. Journal of Geophysical Research-Oceans. 115.
396 Cossu, R., Wells, M., 2013. The evolution of submarine channels under the influence of Coriolis forces: experimental
397 observations of flow structures. Terra Nova. 25, 65-71.
398 Covault, J.A., Kostic, S., Paull, C.K., Ryan, H.F., Fildani, A., Talling, P., 2014. Submarine channel initiation, filling
399 and maintenance from sea-floor geomorphology and morphodynamic modelling of cyclic steps. Sedimentology.
400 61, 1031-1054.
401 Covault, J.A., Kostic, S., Paull, C.K., Sylvester, Z., Fildani, A., 2017. Cyclic steps and related supercritical bedforms:
402 Building blocks of deep-water depositional systems, western North America. Marine Geology. 393, 4-20.
403 de Leeuw, J., Eggenhuisen, J.T., Cartigny, M.J.B., 2016. Morphodynamics of submarine channel inception revealed
404 by new experimental approach. Nat Commun. 7, 10886.
405 Ding, W., Franke, D., Li, J., Steuer, S., 2013. Seismic stratigraphy and tectonic structure from a composite multi-
406 channel seismic profile across the entire Dangerous Grounds, South China Sea. Tectonophysics. 582, 162-176.

Fildani, A., Normark, W.R. Kostic, S., Parker, G., 2006. Channel formation by flow stripping: large-scale scour features along the Monterey East Channel and their relation to sediment waves. Sedimentology. 53, 1265-1287.

Feng, D., Cheng, M., Kiel, S., Qiu, J.W., Yang, Q., Zhou, H., Peng, Y., Chen, D., 2015. Using Bathymodiolus tissue stable carbon, nitrogen and sulfur isotopes to infer biogeochemical process at a cold seep in the South China Sea. Deep Sea Research Part I Oceanographic Research Papers. 104, 52-59.

Gabbard, D.S., Huang, C., Norton, L.D., Steinhardt, G.C., 1998. Landscape position, surface hydraulic gradients and erosion processes. Earth Surface Processes and Landforms. 23, 83–93.

Gavey, R., Carter, L., Liu, J., Talling, P.J., Hsu, R.T., Pope, E., Evans, G., 2016. Frequent sediment density flows during 2006 to 2015, triggered by competing seismic and weather events: Observations from subsea cable breaks off southern Taiwan. Marine Geology - MAR GEOLOGY. 384, 147-158.

Gong, C.L., Wang, Y., Zhu, W., Li, W.G., Xu, Q., Zhang, J.M., 2011. The Central Submarine Canyon in the Qiongdongnan Basin, northwestern South China Sea: Architecture, sequence stratigraphy, and depositional processes. Marine & Petroleum Geology. 28, 0-1702.

Hage, S., M. J. B. Cartigny., M. A. Clare., E. J. Sumner., D. Vendettuoli., J. E. Hughes Clarke., S. M. Hubbard., P. J. Talling., D. G. Lintern., C. D. Stacey., R. G. Englert., M. E. Vardy., J. E. Hunt., M. Yokokawa., D. R. Parsons., J. L. Hizzett., M. Azpiroz-ZabalaA. J. Vellinga., 2018. How to recognize crescentic bedforms formed by supercritical turbidity currents in the geologic record: Insights from active submarine channels. Geology. 46: 563-566.

Hsu, S.K., Kuo, J., Yeh, Y.C., Tsai, C.H., Doo, W., Ku, C.Y., Sibuet, J.C., 2008. Turbidity Currents, Submarine Landslides and the 2006 Pingtung Earthquake off SW Taiwan. AGU Fall Meeting Abstracts. 19, 767.

Huang. C.H., Laflen, J.M., 1996. Seepage and Soil Erosion for a Clay Loam Soil. Science Society of America Journal. 60, 408-416.

429 Jones, O.P., Simons, R., Jones, E., Harris, J.M., 2006. Influence of seabed slope and Coriolis effects on the
430 development of sandbanks near headlands. Journal of Geophysical Research. 111.
431 Komar, P.D., 1969. The channelized flow of turbidity currents with application to Monterey Deep-Sea Fan Channel.
432 Journal of Geophysical Research. 74: 4544-4558.
433 Konsoer, K., Zinger, J., Parker, G., 2013. Bankfull hydraulic geometry of submarine channels created by turbidity
434 currents: Relations between bankfull channel characteristics and formative flow discharge. Journal of
435 Geophysical Research: Earth Surface. 118, 216-228.
436 Kostic, S., Parker, G., 2006. The response of turbidity currents to a canyon-fan transition: Internal hydraulic jumps
437 and depositional signatures. Journal of Hydraulic Research - J HYDRAUL RES. 44, 631-653.
438 Kostic, S., Sequeiros, O., Spinewine, B., Parker, G., 2010. Cyclic steps: A phenomenon of supercritical shallow flow
439 from the high mountains to the bottom of the ocean. Journal of Hydro-environment Research. 3, 167-172.
440 Kostic, S., 2011. Modeling of submarine cyclic steps: Controls on their formation, migration, and architecture.
441 Geosphere. 7, 294-304.
442 Lamb, M.P., Parsons, J.D., Mullenbach, B.L., Finlayson, D.P., Orange, D.L., Nittrouer, C.A., 2008. Evidence for
443 superelevation, channel incision, and formation of cyclic steps by turbidity currents in Eel Canyon, California.
444 Geological Society of America Bulletin. 120, 463-475.
445 Lee, T.Y., Tang, C.H., Ting, J.S., Hsu, Y.Y., 1993. Sequence stratigraphy of the Tainan Basin, offshore southwestern
446 Taiwan. Petroleum Geology of Taiwan. 28, 119-158.
447 Li, C.F., Xu, X., Lin, J., Sun, Z., Zhu, J., Yao, Y., Zhao, X., Liu, Q., Kulhanek, D., Wang, J., Song, T., Zhao, J., Qiu,
448 N., Guan, Y., Zhou, Z., Williams, T., Bao, R., Briais, A., A. Brown, E., Zhang, G.L., 2014. Ages and magnetic
449 structures of the South China Sea constrained by deep tow magnetic surveys and IODP Expedition 349.
450 Geochemistry, Geophysics, Geosystems. 15.

Li, L., Gong, C.L., 2018. Gradual Transition From Net Erosional to Net Depositional Cyclic Steps Along the Submarine Distributary Channel Thalweg in the Rio Muni Basin: A Joint 3-D Seismic and Numerical Approach. Journal of Geophysical Research: Earth Surface. 123, 2087-2106.

Lin, A., Liu, C.S., Lin, C.C., Schnurle, P., Chen, G.Y., Liao, W.Z., S. Teng, L., Chuang, H.-J., Wu, M.-S., 2008. Tectonic features associated with the overriding of an accretionary wedge on top of a rifted continental margin: An example from Taiwan. Marine Geology - MAR GEOLOGY. 255, 186-203.

Liu, J., Chao, Y.S., Hsu, R.T., 1999. The influence of suspended sediments on the plume of a small mountainous river. Journal of Coastal Research. 15, 1002-1010.

Maier, K.L., Fildani, A. Paull, C.K., Graham, S.A., McHargue, T.R., Caress, D.W., McGann, M., 2011. The elusive character of discontinuous deep-water channels: New insights from Lucia Chica channel system, offshore California. Geology. 39, 327-330.

Mchargue T R., 1991. Seismic Facies, Processes, and Evolution of Miocene Inner Fan Channels, Indus Submarine Fan. Seismic Facies and Sedimentary Processes of Submarine Fans and Turbidite Systems. Springer New York.

Mosher, D. C., Campbell, D. C., Gardner, J. V., Piper, D. J. W., Chaytor. J. D., Rebesco. M., 2017. The role of deep-water sedimentary processes in shaping a continental margin: The Northwest Atlantic. Marine Geology. 393: 245-259.

Paull, C., Greene, H., Ussler, B., Mitts, P.J., 2002. Pesticides as tracers of sediment transport through Monterey Canyon. Geo-Marine Letters. 22, 121-126.

Pautot, G., Rangin, C., Briais, A., Tapponnier, P., Beuzart, P., Lericolais, G., Mathieu, X., Wu, J., Han, S., Li, H., Lu, Y., Zhao, J., 1986. Spreading direction in the central South China Sea. Nature. 321, 150-154.

Persson, A., 1998. How Do We Understand the Coriolis Force? Bulletin of the American Meteorological Society. 791, 373-1385.

473 Persson, A., 2000. Back to basics: Coriolis: Part 3 - The Coriolis force on the physical earth. Weather. 55, 234-239
474 Postma, G., Cartigny, M.J.B., Kleverlaan. K., 2009. Structureless, coarse-tail graded Bouma Ta formed by internal
475 hydraulic jump of the turbidity current? Sedimentary Geology. 219, 1-6.
476 Postma, G., Kleverlaan, K., Cartigny, M.J.B., Mohrig, D., 2014. Recognition of cyclic steps in sandy and gravelly
477 turbidite sequences, and consequences for the Bouma facies model. Sedimentology. 61, 2268-2290.
478 Normark, R., Paull, W.C., Caress, D., Ussler, B., Sliter, R.A.Y., 2009. Fine-scale relief related to Late Holocene
479 channel shifting within the floor of the upper Redondo Fan, offshore Southern California. Sedimentology. 56,
480 1690-1704.
481 Rebesco, M., Hernández-Molina, F., Van Rooij, D., Wåhlin, A., 2014. Contourites and associated sediments controlled
482 by deep-water circulation processes: State-of-the-art and future Considerations. Marine Geology - MAR
483 GEOLOGY. 352, 10-12
484 Sibuet, J.C., Hsu, S.K., 1997. Geodynamics of Taiwan arc–arc collision. Tectonophysics 274, 221-251.
485 Symons, W.O., Sumner, E.J., Talling, P.J., Cartigny, M.J.B., Clare, M.A., 2016. Large-scale sediment waves and
486 scours on the modern seafloor and their implications for the prevalence of supercritical flows. Marine Geology.
487 371, 130-148.
488 Spinewine, B., Sequeiros, O., García, M., Beaubouef, R., Sun, T., Savoye, B., Parker, G., 2009. Experiments on
489 Wedge-Shaped Deep Sea Sedimentary Deposits in Minibasins and/or on Channel Levees Emplaced by Turbidity
490 Currents. Part II. Morphodynamic Evolution of the Wedge and of the Associated Bedforms. Journal of
491 Sedimentary Research - J SEDIMENT RES. 79, 608-628.
492 Suppe, J., 1981. Mechanics of mountain building and metamorphism in Taiwan. Memoir of the Geological Society of
493 China (Taiwan). 4, 67-89.
494 Talling, P.J., Wynn, R.B., Masson, D.G., Frenz, M., Cronin, B., Schiebel, R., Akhmetzhanov, A.M., Dallmeier-Tiessen,

S., Benetti, S., Weaver, P., Georgiopoulou, A., Zühlsdorff, C., Amy, L., 2007. Onset of submarine debris flow deposition far from original giant landslide. Nature. 450, 541-544.

Talling, P.J., Masson, G.D., Sumner, J.E., Malgesini, G., 2012. Subaqueous sediment density flows: Depositional processes and deposit types. Sedimentology. 59, 1937-2003.

Taylor, B., E. Hayes, D., 1983. Origin and History of the South China Sea Basin. Washington DC American Geophysical Union Geophysical Monograph Series. 27, 23-56.

Vellinga, A., J.B. Cartigny, M.J.B., Eggenhuisen, J., Hansen, W.M.E., 2017. Morphodynamics and depositional signature of low-aggradation cyclic steps: New insights from a depth-resolved numerical model. Sedimentology. 65, 540-560.

Wang P., Li Q., 2009. The South China Sea - Paleoceanography and Sedimentology. Springer.

Wang, X.J., B. Liu., J. Qian., X. Zhang., Y. Guo., P. Su., J. Liang., J. Jin., Z. Luan., D. Chen., S. XiC. Li., 2018. Geophysical evidence for gas hydrate accumulation related to methane seepage in the Taixinan Basin, South China Sea. Journal of Asian Earth Sciences. 168, 27-37.

Wells, M. G. 2009. How Coriolis forces can limit the spatial extent of sediment deposition of a large-scale turbidity current. Sedimentary Geology. 218: 1-5.

Wynn, R.B., Stow, D., 2002. Classification and characterisation of deep-water sediment waves. Marine Geology - MAR GEOLOGY. 192, 7-22.

Xie, X., Müller, R.D., Li, S., Gong, Z., Steinberger, B., 2006. Origin of anomalous subsidence along the Northern South China Sea margin and its relationship to dynamic topography. Marine and Petroleum Geology. 23, 745-765.

Yin, S., Wang, L., Guo, Y., Zhong, G., 2015. Morphology, sedimentary characteristics, and origin of the Dongsha submarine canyon in the northeastern continental slope of the South China Sea. Science China Earth Sciences.

517 58, 971-985.

518 Yu, H.S., Chiang, C.S., 1994. Morphology and origin of the Hongtsai submarine canyon west of the Hengchun
519 Peninsula, Taiwan. J. Geol. Soc. China. 38, 81-92.

520 Yu, H.S., Hong, E., 2006. Shifting submarine canyons and development of a foreland basin in SW Taiwan: controls of
521 foreland sedimentation and longitudinal sediment transport. Journal of Asian Earth Sciences. 27, 922-932.

522 Zhang, Y., Liu, Z., Zhao, Y., Colin, C., Zhang, X., Wang, M., Zhao, S., Kneller, B., 2018. Long-term in situ
523 observations on typhoon-triggered turbidity currents in the deep sea. Geology. 46, 675-678.

524 Zhong, G., Cartigny, M.J.B., Kuang, Z., Wang, L., 2015. Cyclic steps along the South Taiwan Shoal and West Penghu
525 submarine canyons on the northeastern continental slope of the South China Sea. Geological Society of America
526 Bulletin. 127, 804-824.

527 Notation

528 $\mathbf{A_y}$ asymmetry of cyclic steps, defined as L_{stoss}/L_{lee}

529 **C** volume sediment concentration

530 $\mathbf{C_{fb}}$ coefficient of friction at the bed

531 $\mathbf{C_{fi}}$ coefficient of friction at the interface between the flow and ambient fluid

532 $\mathbf{e_w}$ entrainment rate of ambient water into the current

533 **g** gravitational acceleration

534 **R** $(\rho_{sed}-\rho_w)/\rho_w$ (ρ_{sed} and ρ_w denote the densities of the sediment and clear water, respectively)

535 $\mathbf{R_i}$ Richardson number

536 **S** slope of the canyon

537 $\mathbf{W_1}$ bankfull width at trough

538 $\mathbf{W_3}$ bankfull width at cyclic step crest

539 $\mathbf{W_1/H_1}$ width to depth ratio at trough

540 $\mathbf{W_3/H_3}$ width to depth ratio at cyclic step crest

541 $\mathbf{H_1}$ flow depth before hydraulic jump

542 $\mathbf{H_2}$ flow depth post hydraulic jump

543 $\mathbf{H_3}$ flow depth at step crest

544 $\boldsymbol{\alpha}$ stoss side slope angle

545 $\boldsymbol{\beta}$ lee side slope angle

546 $\boldsymbol{\theta}$ slope angle of cyclic step

547 $\mathbf{L_{stoss}}$ stoss side length

548 $\mathbf{L_{lee}}$ lee side length

549 $\mathbf{L_{step}}$ length of cyclic steps (wavelength)

550 $\mathbf{H_{step}}$ height of cyclic steps (waveheight)

551 $\mathbf{V_1}$ flow velocity before hydraulic jump

552 $\mathbf{V_2}$ flow velocity after hydraulic jump

553 $\mathbf{V_3}$ flow velocity at cyclic step crest

554 $\mathbf{F_{r1}}$ densimetric Froude number before hydraulic jump

555 $\mathbf{F_{r2}}$ densimetric Froude number after hydraulic jump

556 $\mathbf{F_{r3}}$ densimetric Froude number at cyclic step crest

557 $\mathbf{Q_1}$ bankfull discharge before hydraulic jump

558 $\mathbf{Q_3}$ bankfull discharge at cyclic step crest

559 $\boldsymbol{\Delta_{el}}$ energy loss of hydraulic jump

Equations

$$0 = \frac{SC_{fb}^{-1}}{1+\frac{ew(1+0.5R_i)}{C_{fb}}} - \frac{1}{R_i} \quad (1)$$

$$e_w = \frac{0.0075}{\sqrt{1+718R_i^{2.4}}} \quad (2)$$

$$C_{fi} = e_w(1 + 0.5R_i) \quad (3)$$

$$r = \frac{C_{fi}}{C_{fb}} \quad (4)$$

$$V^2 = (\frac{1}{1+r})\frac{RCgHS}{C_{fb}} \quad (5)$$

$$Q = VWH \quad (6)$$

$$F_r = \frac{V}{\sqrt{RCgH}} \quad (7)$$

Where e_w is the dimensionless coefficient of the entrainment of ambient water into turbidity currents; C_{fi} is the coefficient of friction at the surface of the flow; C_{fb} is the coefficient of friction at the canyon bed (ranging from 0.002 to 0.005, as suggested by Konsoer et al., 2013); S denotes the slope of the canyon bed; R is the submerged specific gravity defined as $R = (\rho_{sed} - \rho_w)/\rho_w$, with ρ_{sed} the density of the sediment and ρ_w the density of the clear water; C is the volume sediment concentration (ranging from 0.2% to 0.6%, as suggested by Konsoer et al., 2013); g is gravitational acceleration (9.81m/s^2); and H is the bankfull depth of the canyon.

$$F_{r_2} = \frac{2^{1.5}F_{r_1}}{(\sqrt{1+8{F_{r_1}}^2}-1)^{1.5}} \quad (8)$$

$$H_2 = 0.5H_1(\sqrt{1+8{F_{r_1}}^2}-1) \quad (9)$$

$$V_2 = \frac{H_1V_1}{H_2} \quad (10)$$

Where H_1 is the flow depth of bankfull turbidity currents before hydraulic jumps, F_{r1} and F_{r2} are the Froude number of bankfull turbidity currents before and after the hydraulic jumps, respectively.

$$\Delta_{el} = \frac{(H_2-H_1)^3}{4H1H2} \quad (11)$$

$$L_{jump} = H_1(160tanh(\frac{F_{r_1}}{20}) - 12) \quad (12)$$

Where Δ_{el} is the loss energy of hydraulic jumps, H_1 and H_2 are the flow depth before and after the hydraulic jumps,

582 respectively. L_{jump} is defined as the distance between the front and downstream faces of the jump. F_{r1} is the Froude

583 number of bankfull turbidity currents before the hydraulic jumps.

584

Figures

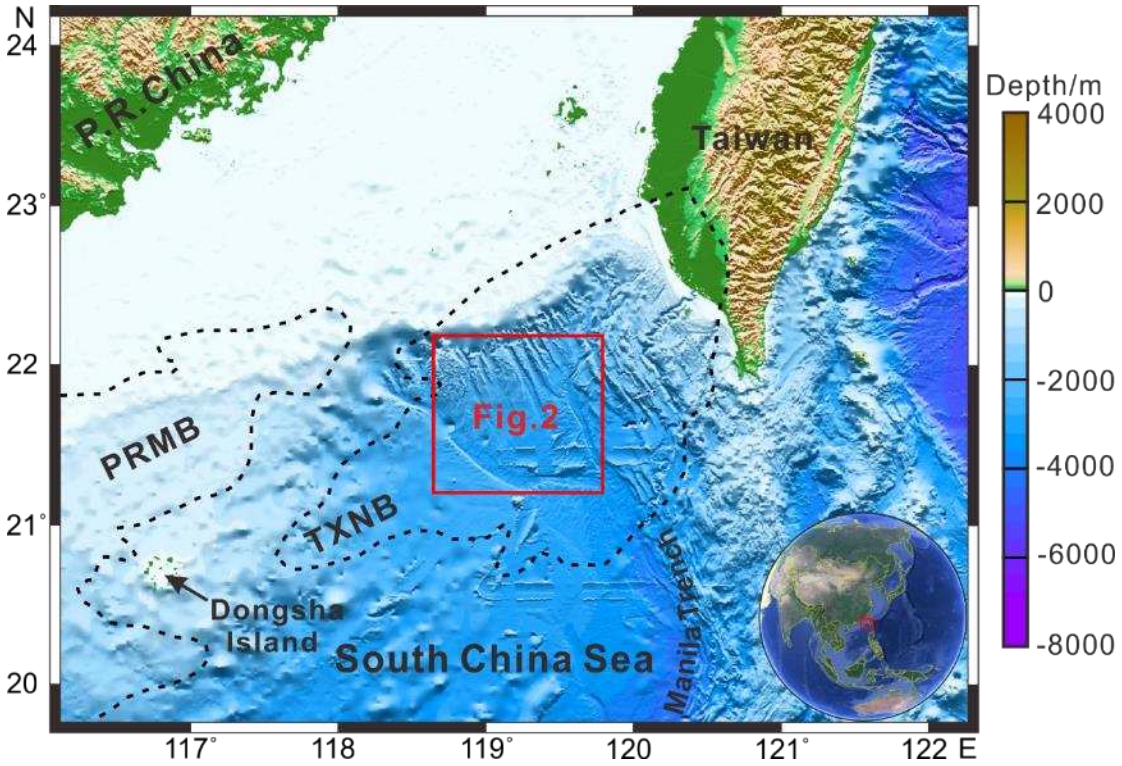

Fig. 1 Regional map of the Taixinan Basin, northeast South China Sea, revealing the detailed location of the study area. The black dotted lines represent the boundaries of the Pearl River Mouth and Taixinan Basins. The red box indicates the location of Figure 2, which lies in the central part of Taixinan Basin. Major bathymetric features, such as the Dongsha Island and the Manila Trench, are marked in the figure. PRMB – Pearl River Mouth Basin; TXNB – Taixinan Basin.

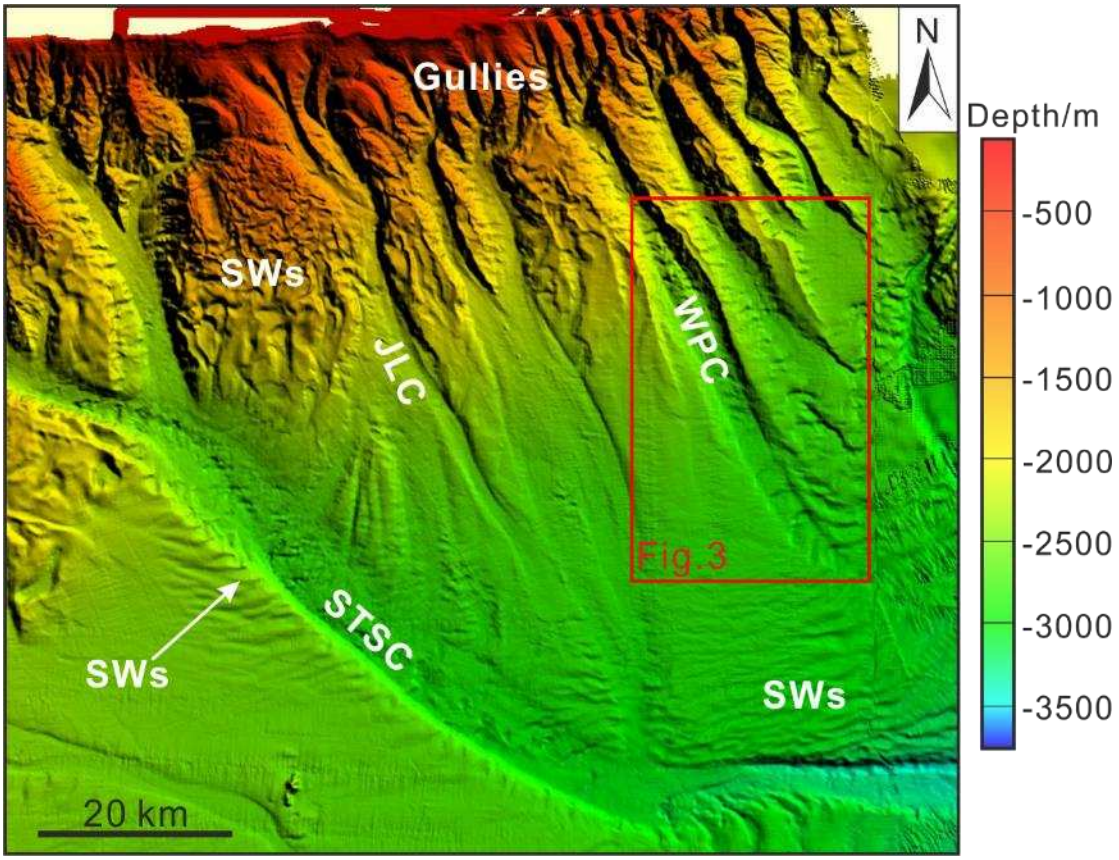

Fig. 2 High-resolution multibeam bathymetric map of the study area showing several submarine canyons with large gullies in their heads. The red box represents the location of Figure 3. Widespread sediment waves can be observed in the downslope region of these submarine canyons. SWs: sediment waves; STSC: South Taiwan Shoal Canyon; JLC: Jiulong Canyon; WPC: West Penghu Canyon.

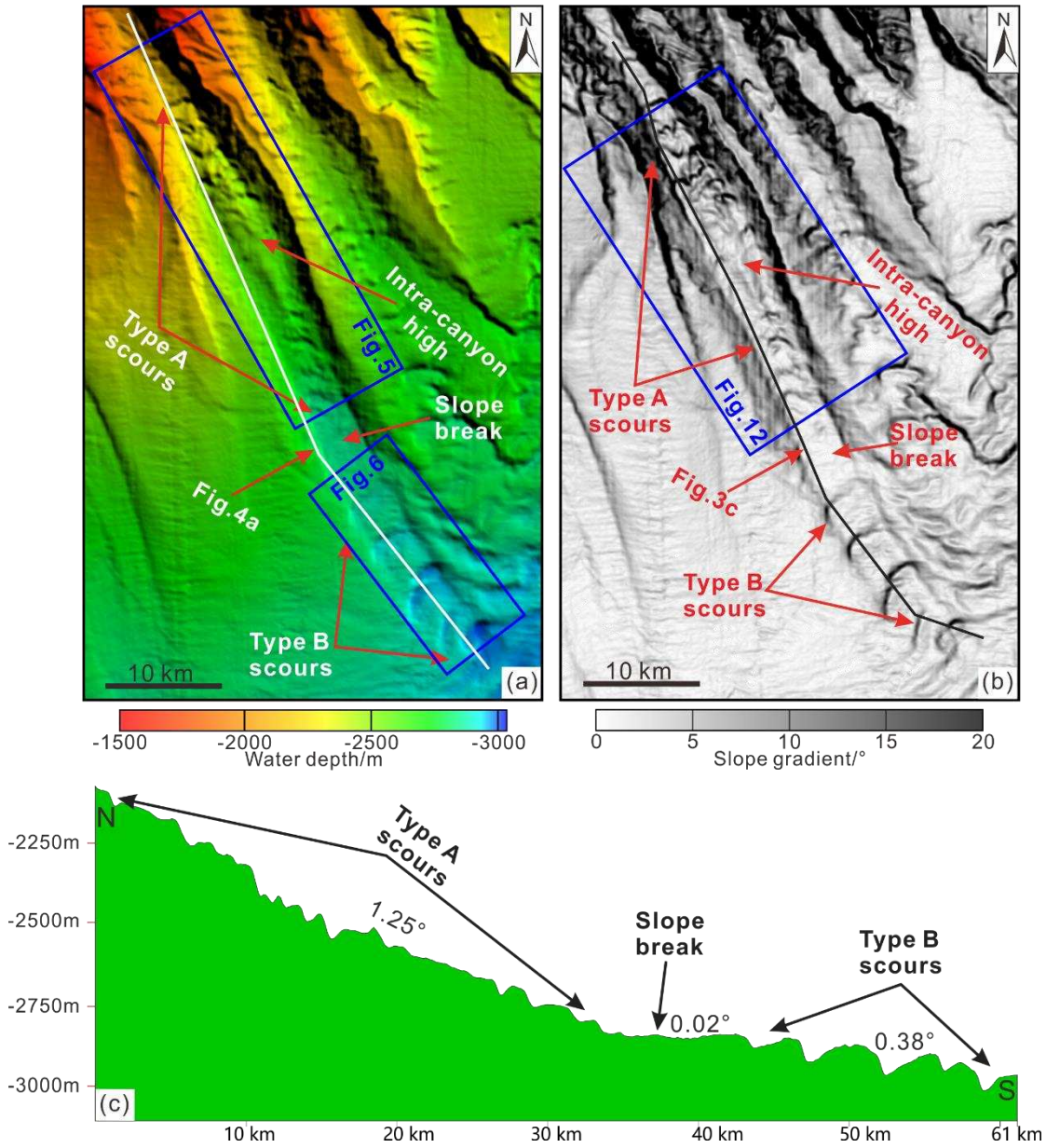

Fig. 3 (a) Multibeam bathymetric map illustrating the morphology and distribution of scours along the thalweg of the West Penghu Canyon (WPC) at a water depth of 1500 m to 3000 m. The blue boxes indicate the areas shown in Figure 5 (Type A scours) and 6 (Type B scours). The white line shows the location of the seismic profile in Figure 4a. A slope break can be identified at a water depth of ~2850 m. (b) Slope gradient map illustrating the morphology of Type A and B scours along the thalweg of the West Penghu Canyon. The blue box indicates the area shown in Figure 12, and an intra-canyon high is marked in this area. The black line indicates the cross-section profile shown in Figure 3c. (c) Bathymetric profile along the thalweg of the West Penghu Canyon showing two different type of scours (Types A and B) separated by a slope break. Note that Type B scours are much larger than Type A scours.

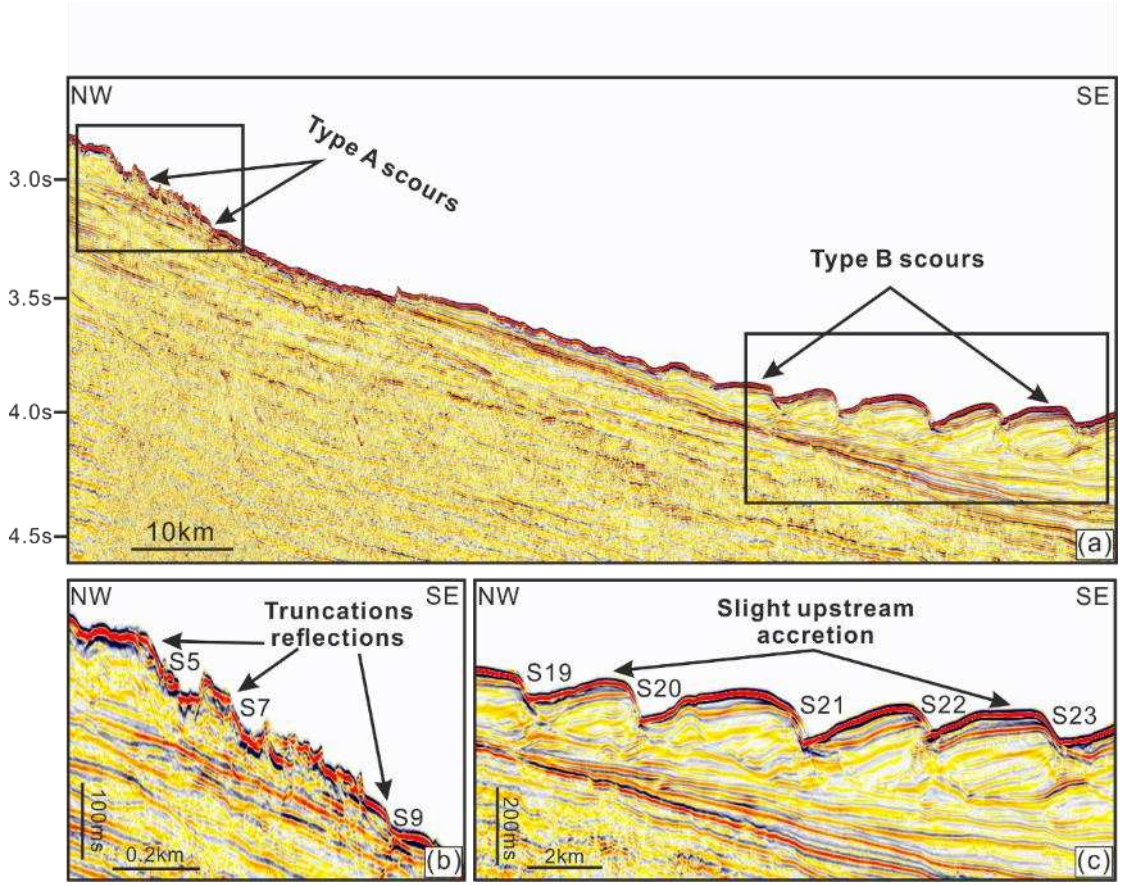

Fig. 4 (a) 2D multichannel seismic profile of the seismic line in Figure 3a. The black boxes indicate the Type A scours and Type B scours shown in Figures 4b and 4c, respectively. (b) Truncated reflections are observed in the stoss sides of Type A scours (S5, S7, S9). (c) Slight upstream accretions are observed in the lee sides of the Type B scours.

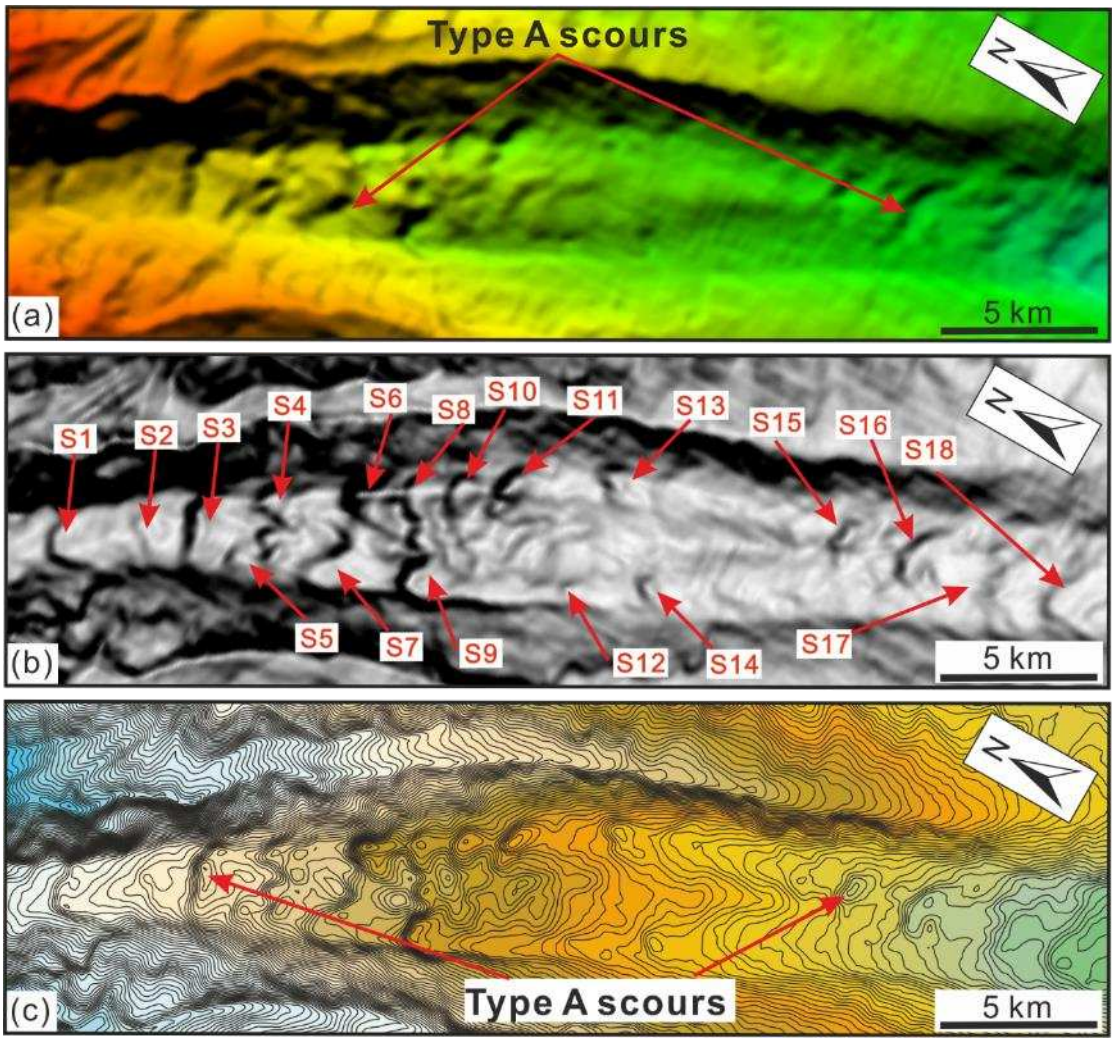

Fig. 5 (a) Multibeam bathymetric map showing the detailed morphology of Type A scours in the upslope region of the West Penghu Canyon. (b) Eighteen (18) Type A scours (S1 to S18) are marked on the slope gradient map from northwest to southeast. (c) The contour map illustrates the distribution of several enclosed depressions, which are interpreted as Type A scours.

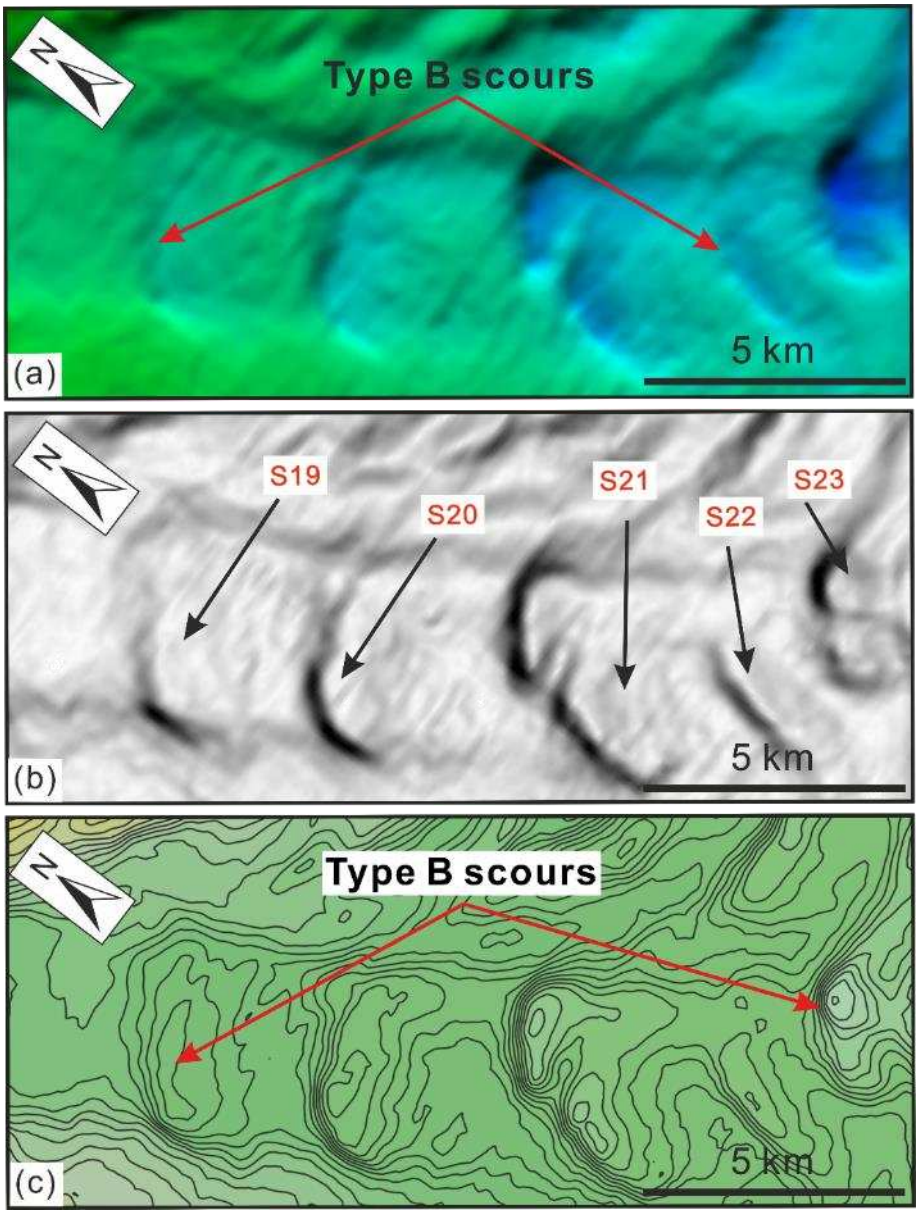

Fig. 6 (a) Multibeam bathymetric map showing the detailed morphology of Type B scours in the deeper, lower-slope region of the West Penghu Canyon. (b) Five (5) Type B scours (S19 to S23) are marked on the slope gradient map from northwest to southeast. (c) The contour map illustrates the distribution of several enclosed depressions, interpreted as Type B scours.

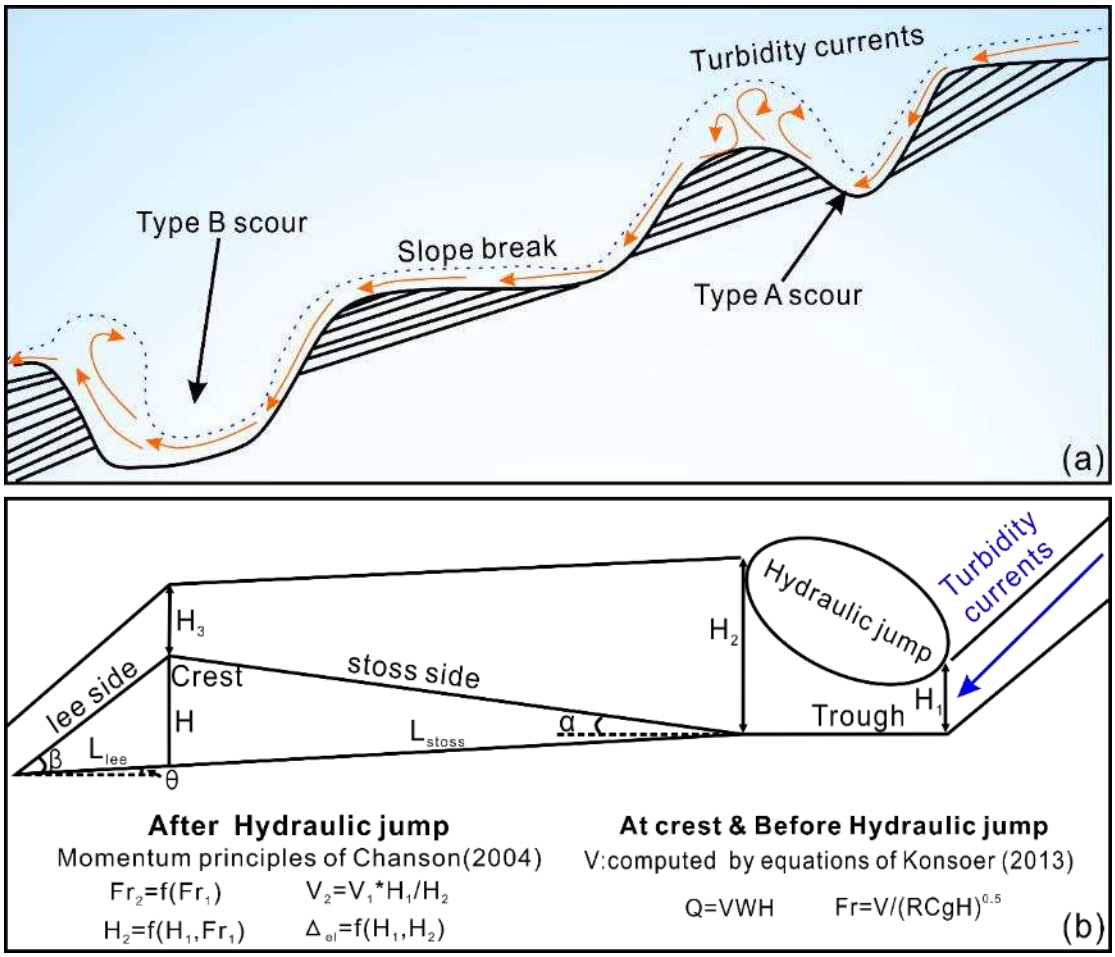

Fig. 7 (a) Schematic diagram depicting the transition from Type A to Type B scours in the region where a slope break is located. The blue dotted line represents the flow depth, while the orange arrows indicate the internal flow structures of overriding turbidity currents (flow is from right to left). (b) Schematic illustration of a single scour showing its morphological parameters (modified by Li and Gong, 2018), and the three locations where the bankfull hydraulics are calculated by using the formulas for turbidity current conditions in this work: (1) at the base of the lee slope just before the hydraulic jump, (2) at the crest of the scour, and (3) at the base of the stoss slope just after the hydraulic jump.

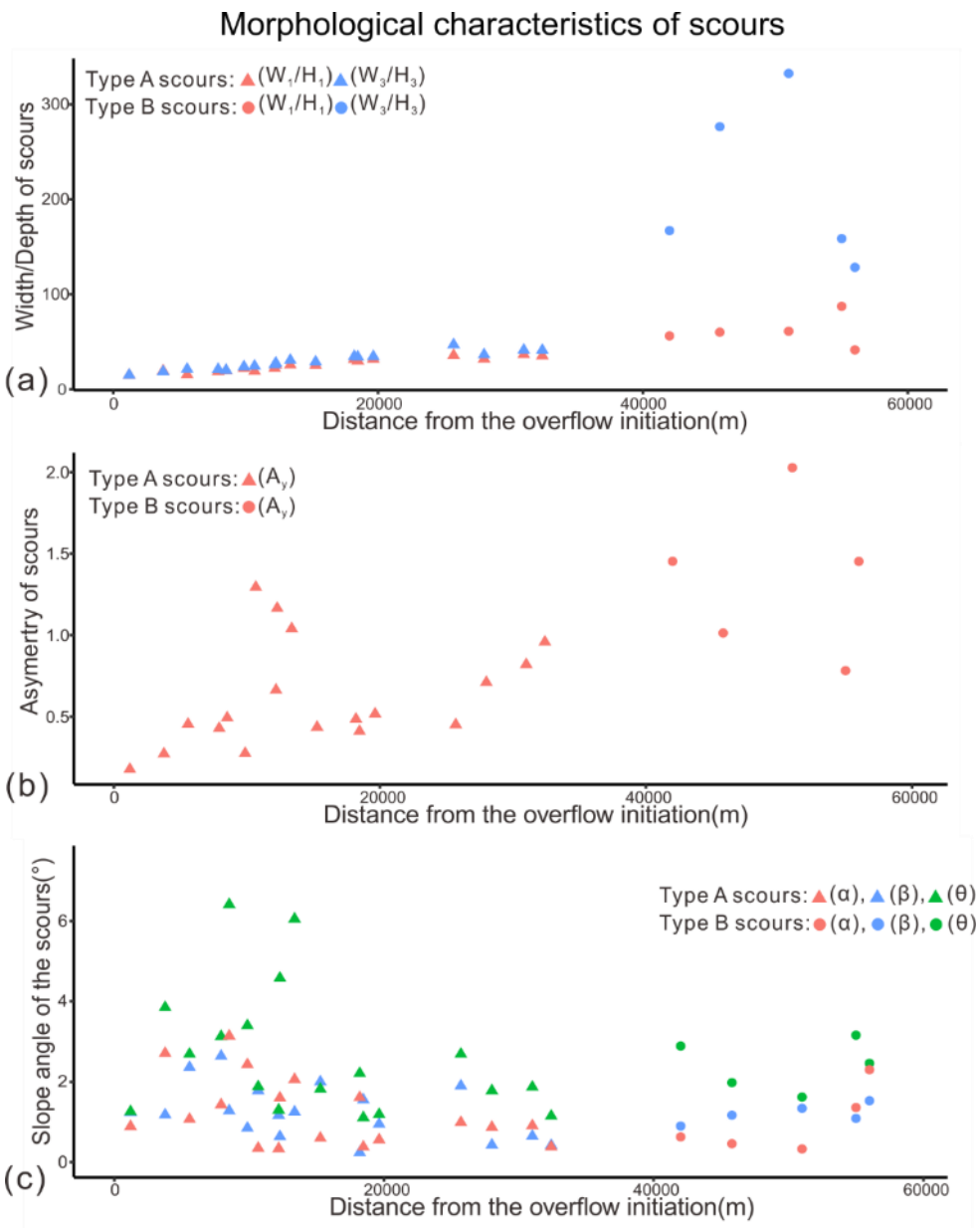

Fig. 8 Morphological characteristics of scours in the West Penghu Canyon. (a) Distance from the overflow initiation vs. W/H. The ratio W_1/H_1 is marked in red, while the ratio W_3/H_3 is indicated in blue. (b) Distance from the overflow initiation vs. A_y. (c) Distance from the overflow initiation vs. slope angle. Slope gradients of the stoss side (α), the lee side (β) and the scour (θ) are marked in red, blue and green, respectively. Note that the triangles represent Type A scours and the circles indicate Type B scours for the three figures above.

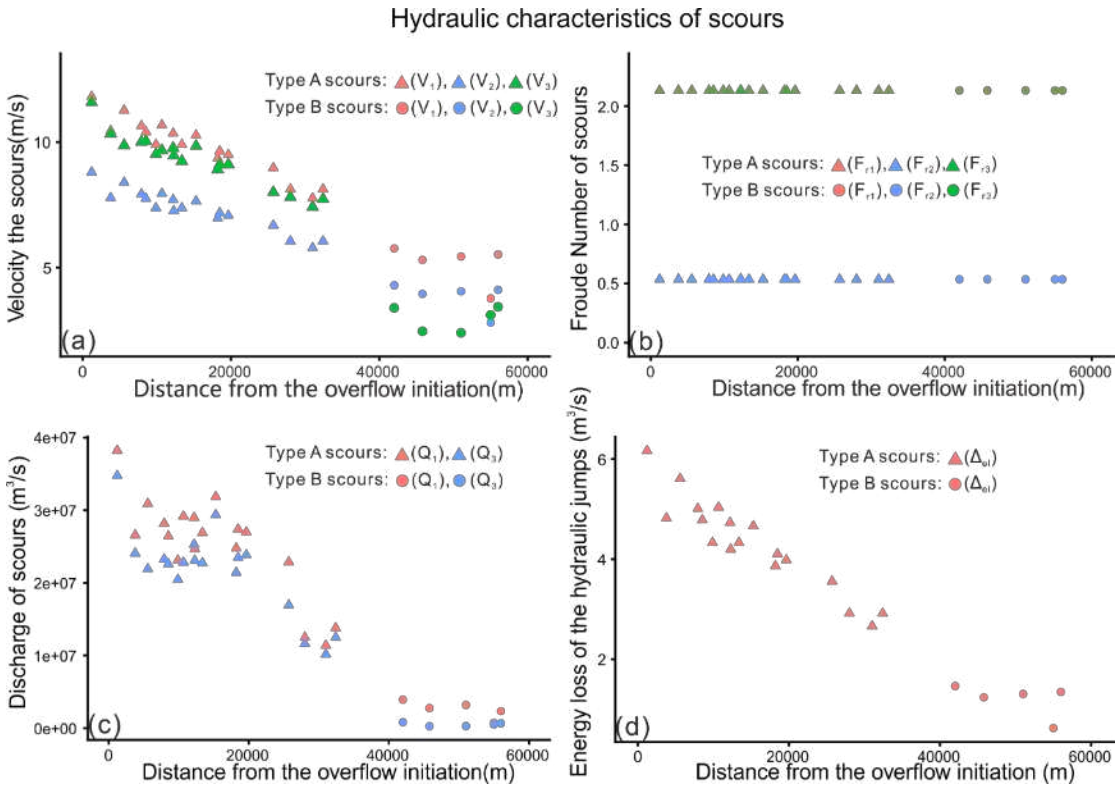

Fig. 9 Hydraulic characteristics of scours in the West Penghu Canyon. (a) Distance from the overflow initiation vs. V, the red represents V_1 (velocity at the trough), the blue represents V_2 (velocity after the hydraulic jumps) and the green symbolizes V_3 (velocity at the crest). (b) Distance from the overflow initiation vs. Fr. Red, blue and green colors denote Fr_1 (Froude number at the trough), Fr_2 (Froude number after the hydraulic jump), and Fr_3 (Froude number at the crest), respectively. (c) Distance from the overflow initiation vs. discharge. In red is Q_1 (discharge at the trough) and in blue is Q_3 (discharge at the crest). (d) Distance from the overflow initiation vs. Δ_{el}. The triangles represent Type A scours and the circles indicate Type B scours.

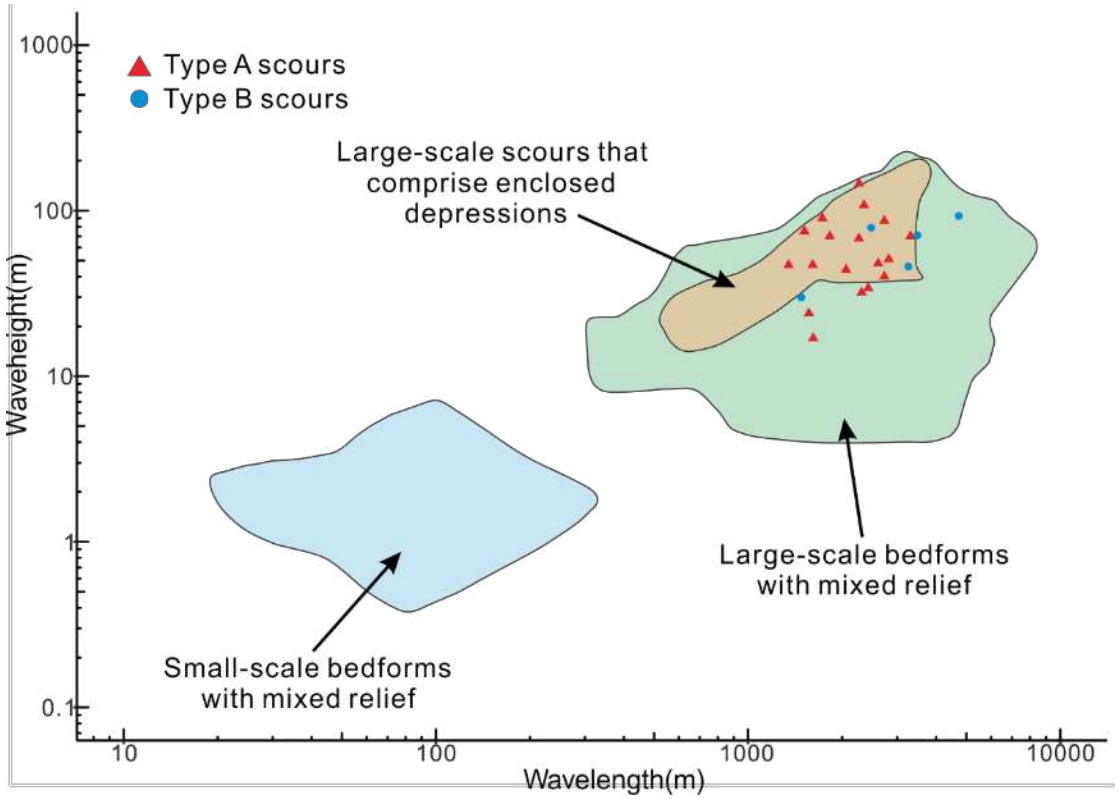

Fig. 10 Logarithmic plots of aspect ratios (wavelength vs. wave height) for twenty-three (23) scours along the thalweg of the West Penghu Canyon, compared to those described in Symons et al. (2016).

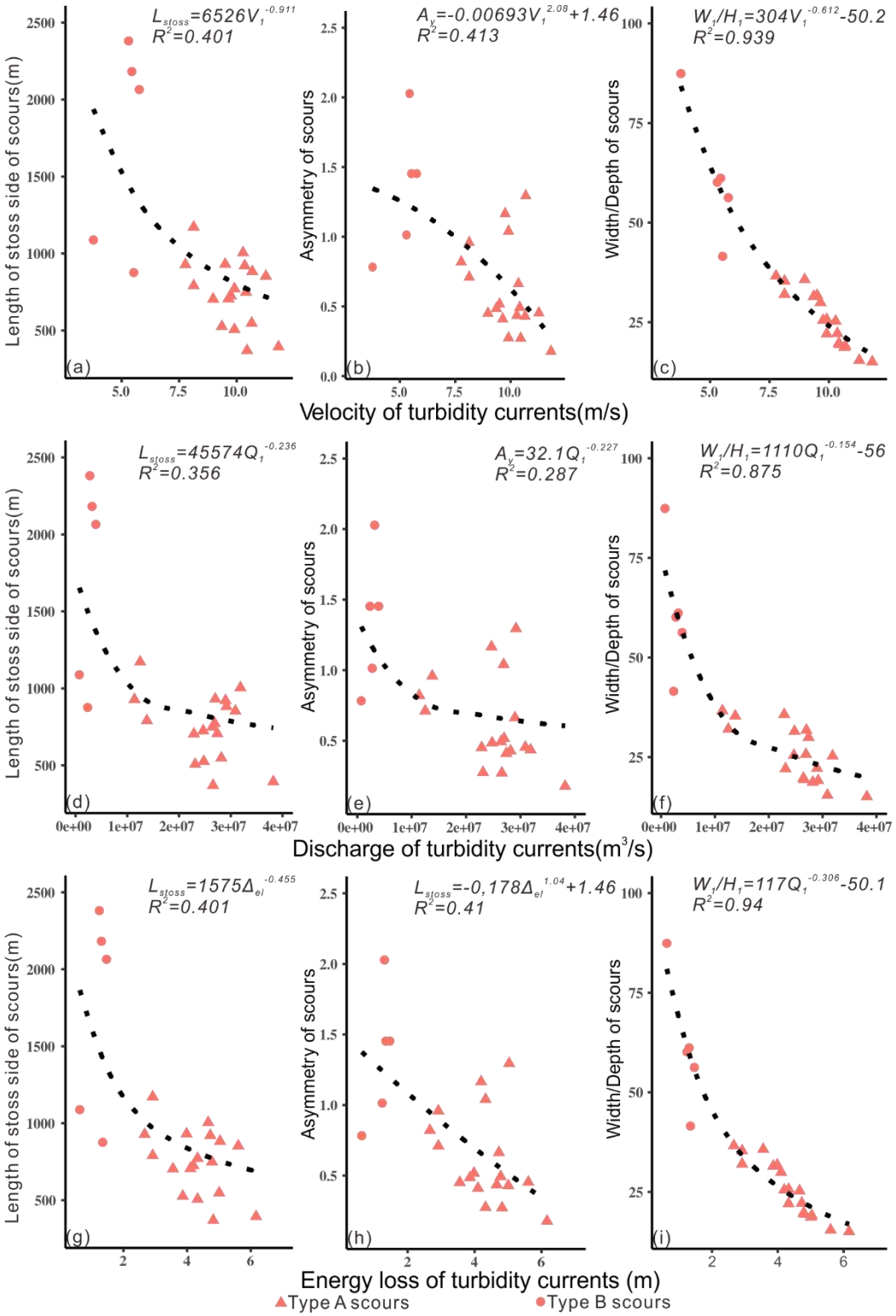

Fig.11 Morphological characteristics and properties of turbidity currents in the West Penghu Canyon, showing relationships of cyclic step morphological characteristics and turbidity current properties. Triangles and circles denote net Type A and B scours, respectively.

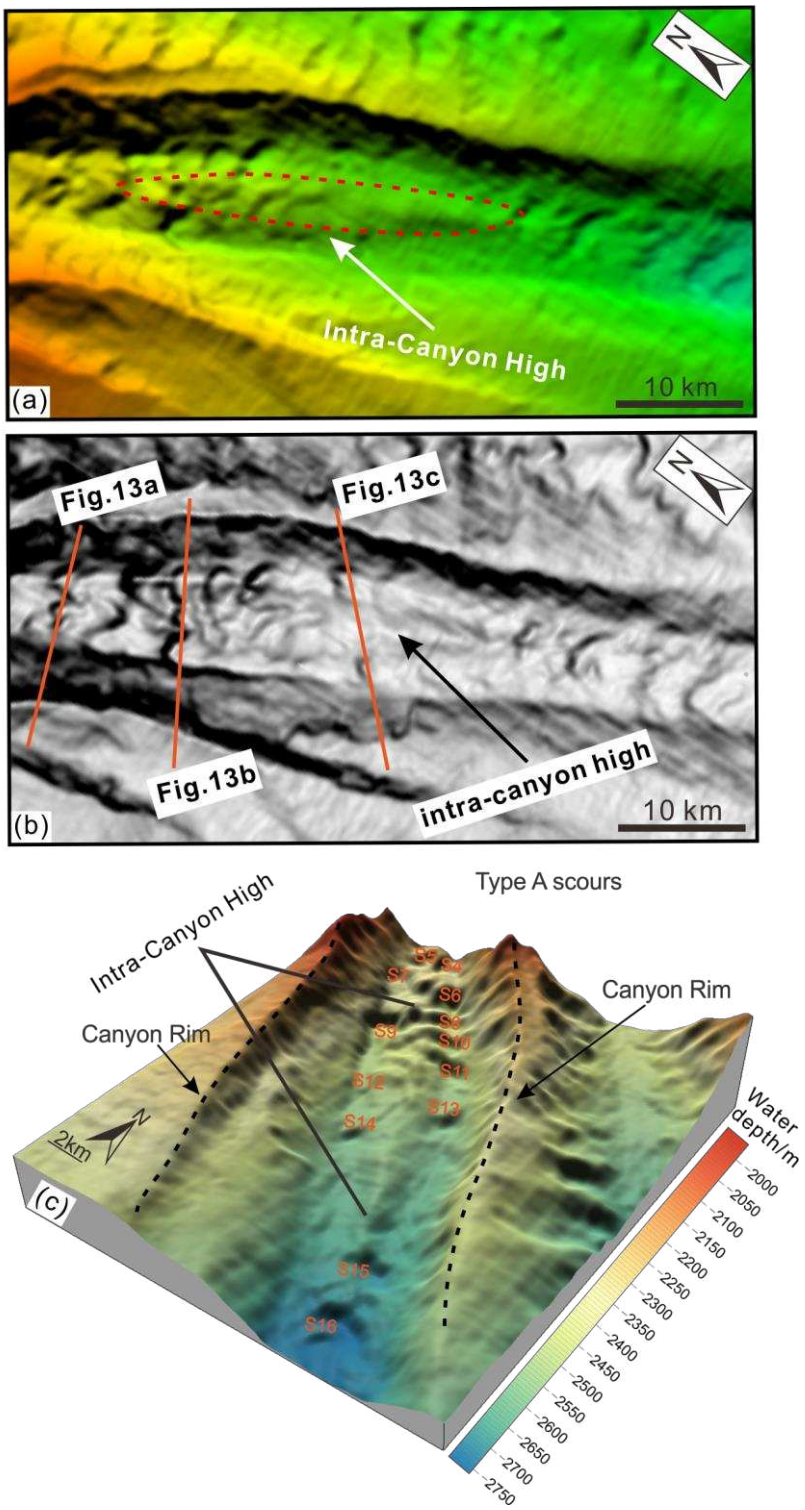

Fig. 12 (a) Multibeam bathymetric map showing the detailed morphology of the intra-canyon high in the upper reach of the West Penghu Canyon. The red dotted line indicates the location of the intra-canyon high at a water depth of 2000 m to 2750 m. (b) The intra-canyon high can also be distinguished on the slope gradient map, while the orange solid lines represent the bathymetric profiles shown in Figures 13a, b and c. (c) 3D perspective view of the upper reach of the West Penghu Canyon showing two trains of Type A scours which are separated by the intra-canyon high.

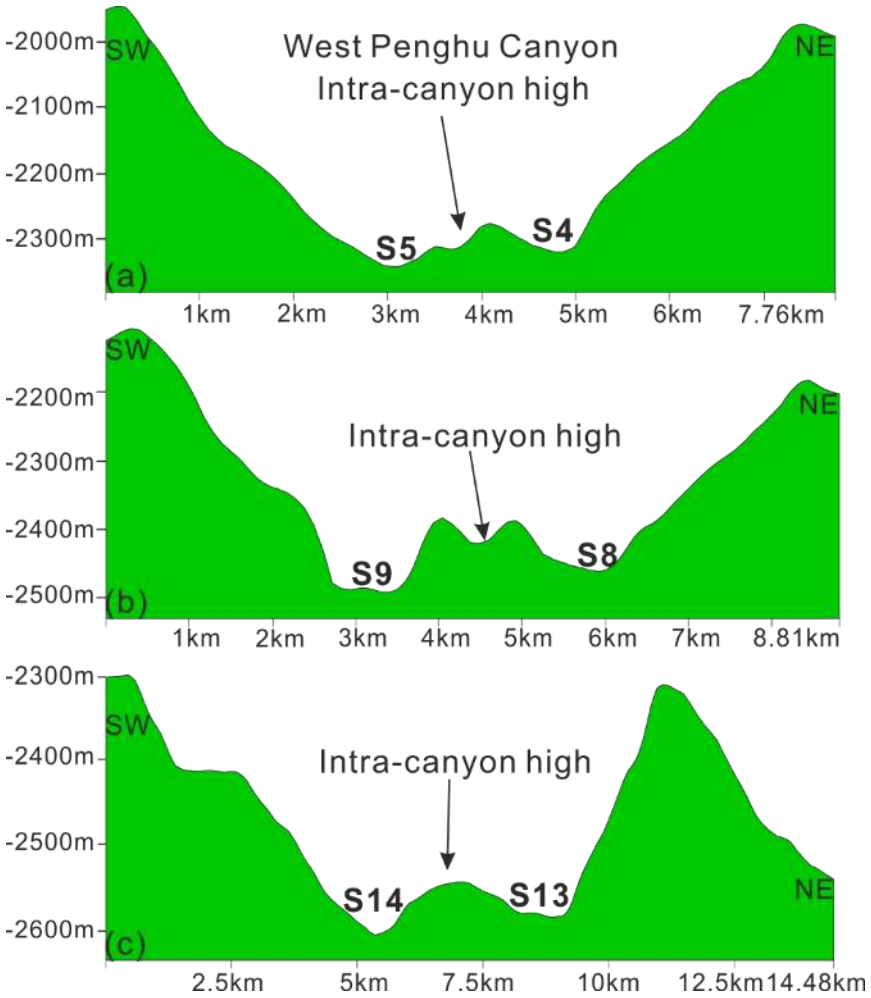

Fig.13 Bathymetric profiles crossing (a) scours 4 and 5, (b) scours 8 and 9, and (c) scours 13 and 14. The profiles show that scours to the southwest of the intra-canyon high are more deeply incised than their counterparts to the northeast.

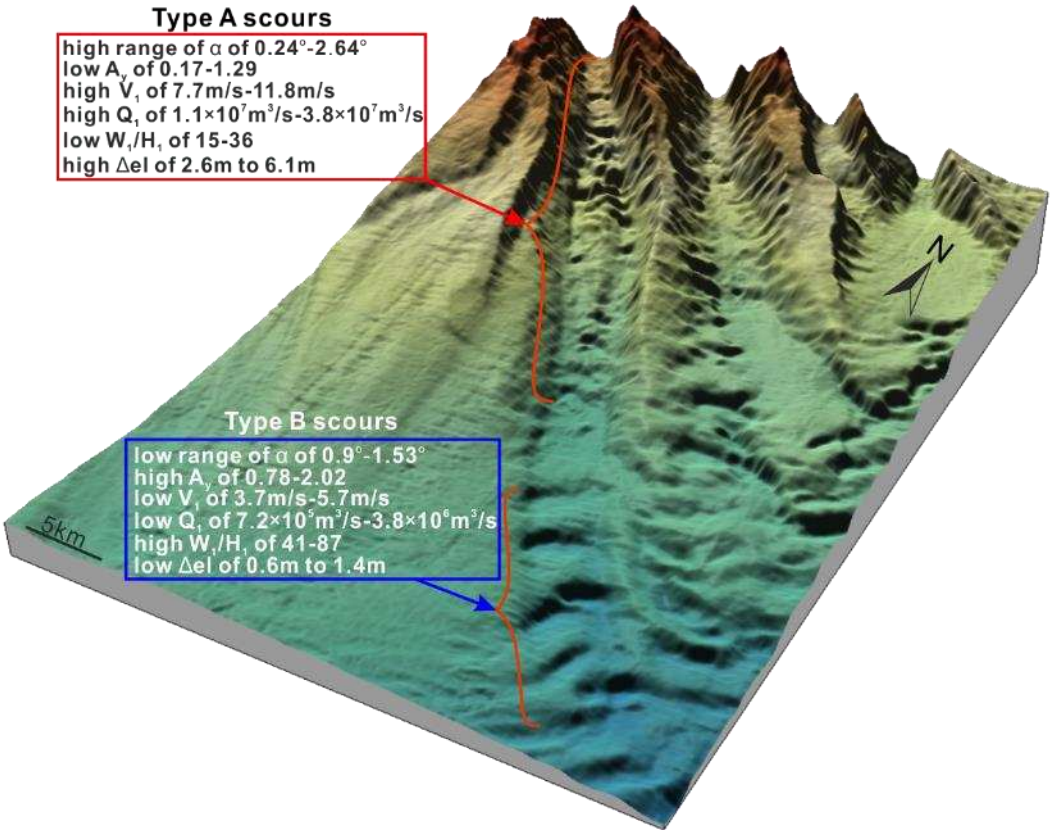

667

668 Fig. 14 3D view of the West Penghu Canyon showing Type A scours in its upper reach and Type B
669 scours in its lower reach. Differences in morphological parameters (Ay, α, and W_1/H_1) and the
670 estimated properties of turbidity currents (V_1, Q_1, and Δ_{el}) are shown in the figure for Type A and B
671 scours.